



HAL
open science

Paleoproterozoic melt-depleted lithospheric mantle in the Khanka block, far eastern Russia: Inferences for mobile belts bordering the North China and Siberian cratons

Dmitri Ionov, Guo Peng, Wendy R. Nelson, Steven B. Shirey, Matthias Willbold

► To cite this version:

Dmitri Ionov, Guo Peng, Wendy R. Nelson, Steven B. Shirey, Matthias Willbold. Paleoproterozoic melt-depleted lithospheric mantle in the Khanka block, far eastern Russia: Inferences for mobile belts bordering the North China and Siberian cratons. *Geochimica et Cosmochimica Acta*, 2020, 270, pp.95-111. 10.1016/j.gca.2019.11.019 . hal-02486520

HAL Id: hal-02486520

<https://hal.umontpellier.fr/hal-02486520>

Submitted on 21 Dec 2021

HAL is a multi-disciplinary open access archive for the deposit and dissemination of scientific research documents, whether they are published or not. The documents may come from teaching and research institutions in France or abroad, or from public or private research centers.

L'archive ouverte pluridisciplinaire **HAL**, est destinée au dépôt et à la diffusion de documents scientifiques de niveau recherche, publiés ou non, émanant des établissements d'enseignement et de recherche français ou étrangers, des laboratoires publics ou privés.



Distributed under a Creative Commons Attribution - NonCommercial 4.0 International License

30 **ABSTRACT** (309 words)

31 The eastern part of Asia between the North China and Siberian cratons contains
32 orogenic belts formed by the Paleo-Asian and Pacific subduction and older continental
33 blocks. A fundamental question regarding these and all mobile belts is the fate of the
34 continental lithospheric mantle (CLM) during their formation, i.e. whether, or to what extent
35 the CLM may be formed, replaced or affected during orogeny. Insights into these processes
36 can be obtained from mantle xenoliths hosted by Cenozoic basalts in the Proterozoic Khanka
37 block in the far eastern Russia between NE China and the Pacific coast of Asia. We report
38 petrographic, chemical, and Os-Sr-Nd isotope data for spinel peridotite xenoliths at two
39 Khanka sites: Sviyagin and Podgelban. The modal abundances and chemical compositions
40 suggest that the peridotites are residues of low to moderate degrees of melt extraction from
41 fertile mantle. They show an $^{187}\text{Os}/^{188}\text{Os}$ vs. $^{187}\text{Re}/^{188}\text{Os}$ correlation with an apparent 1.9 Ga
42 age; the $^{187}\text{Os}/^{188}\text{Os}$ ratios are positively correlated with Al_2O_3 and other melt extraction
43 indices. These results provide the first robust CLM age constraints for the eastern Central
44 Asian Orogenic Belt (CAOB). The ages suggest that the ancient CLM of the Khanka block
45 may be roughly coeval with reworked CLM at Hannuoba (North China craton), and that it
46 persisted through the Phanerozoic orogenies. Moreover, despite the proximity to
47 Phanerozoic subduction zones, the Khanka CLM shows little post-melting enrichment, e.g.
48 the clinopyroxenes are typically LREE-depleted and have Sr-Nd isotope ratios typical of the
49 MORB mantle. We posit that the metasomatism of the CLM, earlier proposed for North
50 China xenolith suites and ascribed to the effects of Pacific or older subduction and related
51 mantle upwelling, may not be widespread in the CAOB. In general, Proterozoic blocks
52 composed of residual peridotites may be more common in the CLM of the SE Siberia and
53 northern China, and possibly other orogenic belts, than previously thought.

54

55

56 **Keywords:** mantle xenolith; peridotite; lithospheric mantle; partial melting; Re-Os isotope;
57 Sr-Nd isotope; metasomatism

58 *7495 words, 2 tables, 9 figures, 69 references; 3 electronic supplements*

59 **1. Introduction**

60 The formation and evolution of the continental lithospheric mantle (CLM), which
61 forms the lower portion of continental plates, is fundamental in the development of Earth's
62 continents. Mantle xenoliths carried to the surface by volcanic eruptions are direct samples
63 of the CLM that may provide valuable insights into its age, composition, structure as well as
64 crust-mantle relations (e.g. [Pearson et al., 2014](#); [Rudnick and Walker, 2009](#); [Walker, 2016](#)).

65 The eastern part of the Asian continent comprises diverse, mainly Phanerozoic, terrains
66 between the North China and Siberian cratons ([Fig. 1](#)). Most of these terrains make up the
67 eastern segment of the Central Asian Orogenic Belt (CAOB) built up by collision and
68 accretion of continental blocks and island arcs during northward subduction and closure of
69 the Paleo-Asian Ocean in the Neoproterozoic to Early Mesozoic (e.g. [Wilde, 2015](#)). The
70 CAOB is separated from the Asian Pacific margin by the Meso-Cenozoic Sikhote-Alin
71 accretionary orogenic belt in far eastern Russia, related to the westward subduction of the
72 Paleo-Pacific plate (e.g. [Zhao et al., 2017](#)).

73 The knowledge of age, composition and structure of the CLM is essential to better
74 understand the multi-stage continental buildup and evolution of eastern Asia, as well as to
75 evaluate the effects of the Paleo-Asian and Pacific subduction on the continental lithosphere.
76 Geophysical and geochemical evidence suggests that the Archean lithospheric mantle of the
77 North China craton was replaced by juvenile mantle at least twice: at around 1.9 Ga in
78 response to collision events in the central craton, then in the Late Mesozoic in its eastern
79 part ([Gao et al., 2002](#); [Liu et al., 2011](#); [Menzies et al., 1993](#)), most likely in relation to
80 westward subduction of the Pacific slab (e.g. [Liu et al., 2019](#); [Xu, 2014](#); [Zhu et al., 2012](#)).
81 Reworking and replacement affected the mantle lithosphere also beneath the central and
82 southeastern (SE) Siberian craton ([Ionov et al., 2005](#); [Ionov et al., 2006a](#); [Ionov et al., 2015](#)).

83 By comparison, the age and composition of the CLM between the North China and
84 Siberian cratons remain poorly constrained, especially due to the paucity of data on the
85 mantle in the far eastern Russia between the northeastern (NE) China and the Pacific coast
86 of Asia. While Cenozoic basaltic rocks hosting mantle xenoliths are widespread in far
87 eastern Russia ([Ionov et al., 1995](#); [Nishio et al., 2004](#)) and NE China ([Xu et al., 1998](#); [Xu et al., 1996](#)) ([Fig. 1](#)), few CLM age estimates were reported for these localities. The estimates

89 that do exist encompass a broad range from Proterozoic to recent and are uncertain because
90 they are based not on isochron dating methods, but on model Re-depletion (Guo et al., 2017;
91 Wu et al., 2003; Zhang et al., 2011, 2019), Sm-Nd and Lu-Hf (Yu et al., 2009) age estimates
92 for individual xenoliths, and are often controversial. Some recent papers invoke replacement
93 of ancient CLM by juvenile materials and/or its extensive reworking often linked to
94 Phanerozoic subduction and recycled oceanic materials (Xu et al., 1996; Zou et al., 2014).
95 However, the nature, distribution and formation processes for the inferred ancient, juvenile
96 and metasomatic CLM components in this vast region remain poorly constrained.

97 Particularly rare are comprehensive data on mantle xenoliths from far eastern Russia.
98 Ionov et al. (1995) reported petrographic and chemical data for eleven peridotite xenoliths
99 from four sites in Sikhote-Alin. Ionov et al. (1999) and Kalfoun et al. (2002) described a few
100 metasomatized xenoliths from northern Sikhote-Alin; Nishio et al. (2004) reported Sr-Nd
101 and Li-isotope data for another five xenoliths. Finally, Guo et al. (2017) provided
102 petro-geochemical and Re-Os isotope data for eight small xenoliths from the Khanka block.

103 In this study, we report on over 30 new, large and fresh peridotite xenoliths from two
104 sites in southern far eastern Russia including petrography, major and trace elements in
105 bulk-rocks and minerals, Sr-Nd isotope compositions for clinopyroxene (cpx), and Os
106 isotope and siderophile element abundances for twelve whole rock peridotites.

107 This work allows us to describe comprehensively the CLM in the Khanka block and
108 constrain its evolution. First, it consists mainly of residual peridotites with rare metasomatic
109 overprints despite the proximity to Phanerozoic subduction zones. Second, the first robust
110 age estimate based on $^{187}\text{Os}/^{188}\text{Os}$ vs. $^{187}\text{Re}/^{188}\text{Os}$ linear correlation is provided for the CLM
111 in far eastern Russia and adjacent NE China. These results are significant also because the
112 crystalline basement does not outcrop in the area and, therefore, it is not possible to
113 constrain its age directly from a crustal section.

114

115 **2. Geological setting and samples**

116 *2.1 Geological background*

117 The continental domain in NE China and southern Siberia between the North China and
118 Siberian cratons (Fig. 1) formed during two major tectonic events: (a) north-south closure of

119 the Neoproterozoic to early Mesozoic Central Asian and the Late Mesozoic
120 Mongol-Okhotsk orogenic belts; (b) westward push related to the Pacific plate subduction
121 that created the Sikhote-Alin Meso-Cenozoic accretionary orogenic belt in far eastern Russia;
122 this geodynamic regime has dominated the regional tectonics since that time (e.g. Liu et al.,
123 2017a). The eastern part of the CAOBS in NE China is commonly referred to as the
124 Xing'an-Mongolian Orogenic Belt (e.g. Xu et al., 2015) and is subdivided into several
125 blocks (massifs); the Khanka block is the easternmost part of the CAOBS that straddles the
126 border with Russia (Fig. 1). All these blocks contain Precambrian rocks and/or detrital
127 zircons and thus may include ancient continental fragments trapped in the CAOBS (Zhou et
128 al., 2018).

129 Cenozoic alkali basalts are widespread both in NE China and in the Russian Primorye
130 (Maritime) region that includes the Sikhote-Alin Mountains and plains near the border with
131 China (Fig. 1). Their origin is linked to continental extension and mantle convection induced
132 by the subduction of the Paleo-Pacific plate (e.g. Okamura et al., 2005).

133

134 2.2 Xenolith localities and samples

135 Mantle xenoliths (Table 1) were collected at two sites in the Khanka block (Fig. 1):
136 Sviyagin (44°80'N, 133°07'E) and Podgelban (43°62'N, 133°05'E). The first site is near the
137 town of Sviyagino east of Lake Khanka, between the Trans-Siberian railway and the Ussuri
138 (A-370) highway. Xenoliths reported in the literature (Guo et al., 2017; Ionov et al., 1995;
139 Wang et al., 2015) are from alkali basalts at the junction of the highway with the road to
140 Sviyagino (Plate 1, Electronic Supplement 1 (ES1)). The basalts may be linked to a nearby
141 ~12 Ma old (Wang et al., 2015) volcanic center composed of tuffs and lava flows containing
142 small (≤ 5 cm) xenoliths; bulk xenolith 8701-4 from this site reported by Ionov et al. (1995)
143 was reanalyzed in this study. In contrast, all new samples in this study are from a basalt
144 quarry south of Sviyagino (ES1) that exposed a ≥ 10 m thick lava flow or pool, which has the
145 largest (10-15 cm) and least altered xenoliths in the area.

146 The Podgelban site is named after a stream in the Arsenievka River basin that crosscuts
147 the NE part of the 9–12 Ma (Okamura et al., 1998) basalts of the Shkotov plateau, SE of
148 Lake Khanka and north of the port of Nakhodka (Fig. 1). The samples are irregular

149 fragments in alkali basalts ~10 cm in size exposed along the stream.

150 Twenty-four Sviyagin and five Podgelban xenoliths were sawed to remove the rinds
151 and thin-sectioned. Twenty of the largest (>100 g) and least altered peridotite samples, as
152 well as a host Sviyagin basalt, were crushed by hammer in plastic sheets and their aliquots
153 ground to powder in agate for whole rock (WR) analyses. Mineral grains were mounted in
154 polished epoxy blocks for in-situ analyses. Essential petrologic and chemical information on
155 the samples is listed in [Table 1](#).

156

157 **3. Methods**

158 Major and minor element compositions of 20 WR samples were determined by
159 wavelength-dispersive X-ray fluorescence (XRF) spectrometry at the Johannes-Gutenberg
160 University, Mainz. The rock powders were ignited for ≥ 3 h at 1000°C, and the loss on
161 ignition (LOI) calculated. Glass beads, produced by fusing 0.8 g of ignited powders with 4.8
162 g of dried LiB₄O₇ were analyzed on a Philips PW 1404 spectrometer using ultramafic and
163 mafic reference samples as external standards. Peridotite reference samples JP-1 and UBN
164 were analyzed as unknowns with results close to recommended values ([Table 1](#), [ES3](#)).

165 Mineral major element compositions were determined by electron probe microanalysis
166 (EPMA) at Montpellier University (MU) on a Cameca SX-100 using 15kV voltage, 15 nA
167 current, counting times of 20–60 s for peaks and background and the ‘X-PHI’ quantification
168 procedure. The modal abundances of the minerals in the rocks were calculated from a
169 least-squares fit of the composition of the WR to its constituent minerals. The totals of the
170 values obtained in the calculations are within $\pm 0.5\%$ of 100%; they are reported normalized
171 to 100%. Equilibration temperatures were calculated using cpx-opx thermometry ([ES2](#)).

172 The trace element concentrations of cpx were determined by laser ablation (LA)
173 inductively coupled mass spectrometry (ICPMS) at the Max-Planck-Institute (MPI) for
174 Chemistry in Mainz in grain mounts using a New Wave UP 213 Nd:YAG laser coupled to a
175 ThermoFinnigan ELEMENT2 sector field. The beam size was 70 μm for cpx and up to 130
176 μm for opx. Trace elements in WR samples were measured by LA-ICPMS on fused glass
177 beads at the MPI for Chemistry. About 130 mg of WR powder and ~10 mg of ultra-pure
178 SiO₂ powder were homogenized to lower the melting temperature of the peridotites. About

179 40 mg of this mixture were molten on an iridium strip heater under Ar atmosphere at ~1550°
180 C, then quenched by switching off the power and a simultaneous blast of cool Ar gas
181 directed onto the lower side of the iridium strip.

182 Handpicked cpx (16–21 mg) from seven samples were acid-leached, dissolved and
183 processed for separation of Sr and Nd prior to isotope analyses on a Triton Thermo-Fisher
184 thermal ionization mass spectrometer (TIMS) at the MPI for Chemistry together with NIST
185 SRM 987 Sr and La Jolla Nd. Mass fractionations were corrected to $^{86}\text{Sr}/^{88}\text{Sr} = 0.1194$ and
186 $^{146}\text{Nd}/^{144}\text{Nd} = 0.7219$. Total procedure blanks are estimated as 46 pg for Sr and 14 pg for Nd.

187 Os isotope compositions and abundances of Re and platinum group elements (PGE) in
188 twelve WR samples were determined at the Department of Terrestrial Magnetism, Carnegie
189 Institution for Science (DTM-CIS). Powder aliquots of ~1.0 g were dissolved at 240°C in a
190 reverse (2:1 HNO₃:HCl) aqua regia solution in Carius tubes (Shirey and Walker, 1995) with
191 ~0.5 g of ^{185}Re - ^{190}Os spike and ~1.5 g of a mixed ^{104}Ru - ^{110}Pd - ^{191}Ir - ^{198}Pt spike. Osmium was
192 removed from the aqua regia solution by a solvent extraction procedure (Cohen and Waters,
193 1996) using CCl₄ and then back-extracted using 9N HBr. Os was loaded from the HBr
194 solution onto Pt filaments and followed when dry with a BaOH activator. Isotopic
195 composition was measured on a Triton TIMS via peak hopping at typical signal sizes of
196 100–400 KCps for ^{192}Os and 3–15 KCps for ^{187}Os , and corrected to $^{192}\text{Os}/^{188}\text{Os} = 3.083$.
197 $^{185}\text{ReO}_3^-$ was monitored for interference corrections, which were negligible for all samples.
198 The average value measured for the DTM standard in the same period was $^{187}\text{Os}/^{188}\text{Os} =$
199 0.17394 ± 0.00008 . Four Os procedural blanks were measured: three of the blanks were <1
200 pg and one was <2 pg, which is negligible (~10³ times lower than in samples in this study).
201 Re, Ru, Ir, Pt, and Pd separates were analyzed using a Nu Plasma high-resolution
202 multi-collector ICPMS. Four procedural blanks for the highly siderophile element (HSE) are
203 as follows: Ir < 1 pg, Ru < 12 pg, Pt < 10 pg, Pd < 5 pg, and Re < 4 pg. Blank corrections
204 are 2.5-8.6% of the measured abundance for Re, but negligible (< 1%) for Ir, Ru, Pt, and Pd.
205 A detailed description of all analytical procedures employed in this study is provided in
206 the ES2. A complete set of analytical data for the samples and reference materials is given in
207 ES3 (Tables 1-6).

208

209 **4. Results**

210 *4.1 Petrography and modal compositions*

211 Modal and WR major oxide compositions were obtained for 17 Sviyagin and three
212 Podgelban xenoliths. All the samples are spinel lherzolites (**Table 1**). Sv-32 has the lowest
213 cpx (6%) and highest olivine (72%), and is close in modal composition to a harzburgite (**Fig.**
214 **2**). The modal ranges in the other 19 samples analyzed in bulk are: 9–17% cpx, 51–66%
215 olivine, 17–30% orthopyroxene (opx), and 1.0–2.5% spinel. The modal ranges for eight
216 Sviyagin peridotites reported by **Guo et al. (2017)** are close to those in this study but show
217 more scatter for cpx (**Fig. 2**), possibly because the modal estimates have more uncertainty
218 due to small size of these samples. No discrete pyroxenite xenoliths or composite peridotites
219 with pyroxenite or other veins have been found.

220 Photomicrographs of six representative Sviyagin xenoliths are given in **Plate 2** of **ES1**.
221 The rocks are medium-grained with texturally equilibrated mineral grains, protogranular,
222 rarely porphyroblastic microstructures, and no strong fabric. The xenoliths show no
223 evidence for invasion of host magma. A few of them have intergrowths of spinel and
224 pyroxenes, cpx with spongy rims or, rare, tiny, fine-grained patches near spinel and cpx that
225 contain silicate glass, feldspar, and Fe-Ti oxides. The xenoliths have no phlogopite or
226 amphibole; olivine-rich Sv-32 has fine-grained apatite that contains 0.9% SrO, 3.6% Cl and
227 0.7% F (**Ionov et al., 2006b**). No sulfides have been found in the xenoliths in this study by
228 optical inspection of polished thin sections in reflected light at normal to medium
229 magnification.

230 Equilibration temperatures (T) for the Sviyagin samples (**Table 1**) define a broad range
231 from 810 to 1000°C. This contrasts with significantly higher T's (993–1054°C) for the
232 Podgelban xenoliths, which appear to come from a hotter (hence probably deeper) CLM
233 section, although the T ranges at both localities overlap at ~1000°C.

234

235 *4.2 Chemical composition of whole-rocks and minerals*

236 The WR major element data for 20 peridotites in this study are given in **ES3 (Table 1)**.
237 They have low loss on ignition (LOI, -0.48 to 0.43 wt.%), consistent with low or negligible
238 alteration from petrographic observations. Positive LOI values in the majority of the samples

239 mean that mass gain due to oxidation of FeO to Fe₂O₃ is greater than the loss of volatiles.
240 Oxide co-variation plots with Al₂O₃ (a melt extraction index) are shown in [Fig. 3](#) and [Plate 3](#)
241 of [ES1](#). Al₂O₃ is negatively correlated with MgO and NiO concentrations and Mg# (molar
242 Mg/(Mg+Fe)), is positively correlated with CaO, Na₂O, TiO₂ and to a lesser degree SiO₂
243 concentrations, and is not correlated with Cr₂O₃. High K₂O (0.03–0.11 wt.%) in six WR
244 samples may be linked to minor amounts of interstitial silicate glass, microcrystalline
245 feldspar and spongy cpx rims ([Plate 2](#) of [ES1](#)).

246 None of the xenoliths have very fertile compositions overlapping primitive mantle (PM)
247 estimates, unlike for peridotite suites from Tariat and Vitim ([Carlson and Ionov, 2019](#); [Ionov,](#)
248 [2002](#)) in the central CAOB; however, some appear only mildly depleted ([Fig. 3](#)). The three
249 Podgelban peridotites have higher modal cpx ([Fig. 4d](#)) and concentrations of Al₂O₃, CaO,
250 Na₂O and TiO₂ than most Sviyagin xenoliths in this study ([Fig. 3](#)), though the number of the
251 samples is too small for conclusive inferences on rock type proportions and compositions at
252 the two sites. They are distinct in composition from five refractory peridotites (8803-1 to
253 8803-5) mistakenly reported by [Ionov et al. \(1995\)](#) as Podgelban samples because of
254 labeling error.

255 An enigmatic feature of the Sviyagin xenolith suite is the unusually high concentrations
256 of P₂O₅ (0.04–0.15 wt.%) in eleven WR peridotites. They cannot be due to contamination by
257 host magma because of insufficiently high P₂O₅ (0.88 wt.%; [ES3](#)) in the host basalt, and the
258 absence of correlations with Na, Al and other elements enriched in the basalt. Sample Sv-32
259 has the highest P₂O₅ and contains accessory apatite ([Plate 2e](#), [ES1](#); [Ionov et al., 2006b](#)) but,
260 based on petrographic data, its modal abundance cannot be as high as 0.4% estimated from
261 P₂O₅ in the WR (0.15 wt.%) and in the apatite (43 wt.%). In addition to optical microscopy,
262 phosphates in five P₂O₅-rich (≥0.08%) xenoliths were sought using EPMA element mapping
263 in stage scanning mode registering signals for P and BSE images ([Ionov et al., 2006b](#)). The
264 mapping found microcrystalline phosphates forming crosscutting and interstitial veins and
265 pockets suggesting they are secondary. They are similar to apatite in major oxide proportions,
266 but distinct from mantle phosphates by very low totals (<90%) and low concentrations of Na,
267 Cl and La (≤0.02%), yet have high F (1.8%) and SrO (1.9%) ([Ionov et al., 2006b](#)).

268 Major element compositions of minerals in 23 Sviyagin and five Podgelban peridotites

269 are given in **Table 2** of **ES3**. Mg# of olivine (Mg#_{Ol}), the major mineral host of Mg and Fe in
270 whole rocks, shows a uniformly close-fitting correlation with the Mg#_{WR} (**Fig. 4a**),
271 demonstrating high accuracy and reproducibility of the data obtained by different methods.
272 The Cr# (molar Cr/(Cr+Al)) of spinel is positively correlated with Mg#_{Ol} (**Fig. 4b**) and
273 negatively correlated with WR Al₂O₃ (**Fig. 4c**) and TiO₂ in cpx. Altogether, the major
274 element variations are consistent with melt extraction trends (e.g. **Carlson and Ionov, 2019**;
275 **Herzberg, 2004**; **Pearson et al., 2014**).

276 The major element ranges for eight Sviyagin peridotites reported by **Guo et al. (2017)**
277 are similar to those in our collection. Most of the samples from the previous work plot with
278 moderately fertile peridotites in this study and, in some cases, deviate slightly from the
279 trends defined by our samples (**Figs. 2–4**). The WR differences may be related to smaller
280 size and greater alteration of the samples in the earlier work.

281

282 *4.3 Trace element composition of whole-rocks and minerals*

283 Trace element compositions for 20 WR samples, cpx from 24 samples and opx from 14
284 samples are given in **Tables 3** and **4** of **ES3**. The WR concentrations of Yb (**Fig. 3f**) and
285 other heavy rare earth elements (HREE) correlate positively with Al₂O₃ indicating a
286 coherent behavior of moderately incompatible major and trace elements usually attributed to
287 the loss of a melt (**McDonough and Sun, 1995**). In contrast, the concentrations of trace
288 elements more incompatible than medium REE (MREE) show broad variations usually
289 unrelated to those of less incompatible elements; when normalized to primitive mantle (PM)
290 they define complex patterns with common positive U and Sr abundance anomalies (**Fig.**
291 **5a,b**).

292 The cpx show parallel and similar patterns of more or less strong depletions in the light
293 REE (LREE) relative to the MREE and the HREE (**Fig. 5c**); the only exception is sample
294 Sv-17, in which both the cpx and the WR are LREE-enriched. Many cpx show slight
295 enrichment of the MREE over the HREE caused by the greater partitioning of the HREE
296 into opx, which is more obvious in samples with high modal opx/cpx ratios (e.g., Sv-32; see
297 opx data below). Extended primitive mantle-normalized trace element patterns for cpx (**Fig.**
298 **5d**) show complex relations for highly incompatible elements with negative anomalies for

299 the high field strength elements (HFSE) Ti, Zr, Hf, Nb and Ta, strong positive anomalies for
300 U, and positive or negative anomalies for Sr. Samples Sv-7 (LREE-depleted) and Sv-17
301 (LREE-enriched) were selected for pyroxene analyses across grains in thin section (18
302 analyses for cpx Sv-7) to check their homogeneity. No core-rim differences have been found
303 in the cpx and opx grains in these samples indicating that inter-mineral chemical
304 equilibration has accompanied textural equilibration.

305 Primitive mantle-normalized REE patterns for opx (Fig. 6a) are smooth with steeper
306 HREE-LREE slopes than for the cpx while extended PM-normalized trace element patterns
307 (Fig. 6b) show significant positive anomalies for the HFSE that match (much weaker)
308 negative anomalies of these elements in coexisting cpx. The opx/cpx elemental ratios (Fig.
309 6c,d) show narrow ranges suggesting that the pyroxenes are in chemical equilibrium with
310 one another and with the bulk rocks (except for the highly incompatible Th, U, Nb, Ta that
311 normally are very low in opx, but may show spurious values due to micro-inclusions and
312 analytical challenges at very low concentrations).

313

314 *4.4 Os-Sr-Nd isotope compositions, and PGE and Re concentrations*

315 The $^{87}\text{Sr}/^{86}\text{Sr}$ and $^{143}\text{Nd}/^{144}\text{Nd}$ ratios for cpx from seven xenoliths are given in Table 5 of
316 ES3. They plot in the depleted segment of the mantle array (Fig. 7) because they have lower
317 $^{87}\text{Sr}/^{86}\text{Sr}$ (0.7023–0.7041) and higher $^{143}\text{Nd}/^{144}\text{Nd}$ (0.5128–0.5133) than the PM (BSE). Five
318 cpx are close to the DMM end-member in the MORB field (as well as three Sviyagin cpx
319 reported by Nishio et al. (2004)); two cpx (Sv-7 and Sv-32) are in the OIB field because of
320 lower $^{143}\text{Nd}/^{144}\text{Nd}$ (0.51284–0.51288) and higher $^{87}\text{Sr}/^{86}\text{Sr}$ (0.7036–0.7041) than the former;
321 these two samples are close in isotopic composition to the host Sviyagin basalt.

322 HSE concentrations and Os isotope ratios for twelve WR samples in this study are given
323 in Table 2 and in Table 6 of ES3. The PGE+Re patterns (Fig. 8) are nearly parallel and show
324 continuous depletions from Ir to Pt, Pd and Re (excepting two samples with minor Re
325 enrichments); seven Sviyagin xenoliths reported by Guo et al. (2017) show similar patterns.

326 The Os concentrations range from 1.0 to 2.9 ppb; their mean (1.9 ± 0.9 ppb, 2σ) is close
327 to those reported for off-craton peridotite xenolith suites erupted by alkali basalts worldwide
328 (e.g. Pearson et al., 2004). The Os concentrations and Os/Ir ratios in the Sviyagin suite are

329 low relative to PM (Becker et al., 2006), which is also seen in many off-craton peridotite
330 xenolith suites (Luguet and Reisberg, 2016; Rudnick and Walker, 2009). The loss of Os has
331 been attributed to processes ranging from metasomatism and melt percolation in the mantle
332 to sulfide breakdown or alteration during and after the transport, yet the Os isotopic ratios
333 typically can remain unmodified by any of these processes (e.g. Reisberg et al., 2005).

334 The samples in this study show a positive $^{187}\text{Os}/^{188}\text{Os}$ vs. $^{187}\text{Re}/^{188}\text{Os}$ linear correlation
335 ($^{187}\text{Os}/^{188}\text{Os} = 0.032 \times ^{187}\text{Re}/^{188}\text{Os} + 0.1148$). The array of data corresponds to general age of
336 1.91 Ga (Fig. 9a). To assess the uncertainty of this age pairs of lines were drawn parallel to
337 the correlation: (a) through the upper and lower samples most remote from the correlation
338 line (crossing $^{187}\text{Os}/^{188}\text{Os}$ axis at ~ 0.118 and 0.112 , Fig. 9a); (b) comprising ten out of
339 twelve samples; the latter cross $^{187}\text{Os}/^{188}\text{Os}$ axis at ~ 0.1165 and 0.113 corresponding to an
340 age range of 2.25 and 1.78 Ga. We prefer to evaluate the data this holistic way rather than to
341 use an isochron regression program because isochron regression programs are best suited to
342 better correlated data arrays with low MSWD values. Using such programs with data arrays
343 that have some scatter (high MSWD values) forces unsupported choices of which analyses
344 to leave out of the regressions and then produces regression errors that may little geologic
345 meaning when applied to the regressed age.

346 We believe that this age estimate is generally robust because the Os isotopic variation
347 can be explained by Re decay and the $^{187}\text{Os}/^{188}\text{Os}$ ratios also define very tight-fitted linear
348 correlations with CaO ($r^2 = 0.96$), MgO ($r^2 = 0.91$), Mg# ($r^2 = 0.90$), Al_2O_3 ($r^2 = 0.86$) and
349 modal cpx ($r^2 = 0.92$) (Fig. 9c-d). Therefore, essential chemical and modal indices of the
350 extent of melt extraction also control the Re/Os ratios in the melting residues and the
351 ingrowth of radiogenic Os with time. Combining our samples with six Sviyagin xenoliths
352 reported by Guo et al. (2017) (excepting a sample with anomalously high $^{187}\text{Re}/^{188}\text{Os}$ of 0.77)
353 yields grouped age of 1.8 Ga and $r^2 = 0.95$ for the overall $^{187}\text{Os}/^{188}\text{Os}$ correlation with CaO.
354 These age estimates agree well with the average T_{MA} of 1.95 Ga for Sviyagin samples in this
355 study if a single sample with an anomalously high T_{MA} is omitted from consideration as well
356 as with the median T_{MA} of 2.1 Ga (Table 2).

357

358 5. Discussion

359 *5.1 The role of melt extraction and metasomatism in the origin of the Khanka peridotites*

360 The CLM is believed to form from the convecting upper mantle, usually following
361 large-scale melt extraction events. The partial melting conditions can be assessed from
362 modal and chemical compositions of residual peridotites in comparison with experimental
363 data on melting of fertile mantle. Plots of Al₂O₃ vs. FeO (Fig. 3a) in melting residues may
364 constrain both pressure (P) and melting degrees because Al₂O₃ is a robust melt extraction
365 index while FeO concentrations are controlled by pressure (Herzberg, 2004). The majority
366 of the Khanka peridotites experienced low to moderate ($\leq 20\%$) batch melting whereas two
367 samples experienced 25–28% melting. The FeO variations in the Khanka xenoliths (Fig. 3a)
368 suggest melting in a broad P range, mainly ≤ 1 GPa to 3 GPa, and up to 4 GPa for three rocks.
369 The equilibration temperatures (hence depth of origin) for the Khanka xenoliths (810–
370 1054°C) range broadly, and do not correlate with Al₂O₃, other melting indices or FeO,
371 suggesting no compositional stratification of the CLM under this region.

372 An alternative way to evaluate melting degrees is to model the WR abundances of
373 moderately incompatible trace elements, e.g. HREE (Plate 5, ES3) that are sensitive to melt
374 extraction and least affected by metasomatism, during melting of fertile mantle (PM) based
375 on mineral-melt partition coefficients and modal compositions. The model used here (Ionov
376 et al., 2017; Takazawa et al., 2000) yields melting degrees of $\sim 15\%$ for the most refractory
377 xenolith Sv-32 and 1–10% for other Khanka samples. These are the lowest possible melting
378 degrees because the model uses incremental fractional melting at 1% steps, which extracts
379 incompatible elements more effectively than batch partial melting in experimental work that
380 provided major oxide indices of melting degrees (Herzberg, 2004) (Fig. 3a).

381 The sum of compositional data on the Khanka peridotites in this study is remarkably
382 consistent with an origin of these rocks by low to moderate degrees of melt extraction from
383 fertile mantle, with no or only minor post-melting effects. This inference is supported by
384 well-fitting correlations of modal and major oxide WR compositions, mineral compositions,
385 a coherent behavior of moderately incompatible major and trace elements (Figs. 3-4) as well
386 as similarities to xenolith suites with proven melt extraction origins like Tariat in Mongolia
387 (central CAOB) (e.g. Carlson and Ionov, 2019).

388 An outstanding feature of the Khanka peridotites in this study is that the co-variation

389 plots for TiO_2 and Na_2O with Al_2O_3 (Fig. 3d-e) and MgO have convex downward shapes (in
390 particular if forced through the PM composition). This is consistent with melting trends
391 calculated from experimental data (Takazawa et al., 2000) and thus suggests little or no
392 overprinting by silicate-melt metasomatism. In contrast, the trends observed in most other
393 worldwide peridotite suites are linear or vague (Rudnick and Walker, 2009) and thus may
394 signify late-stage melt entrapment or addition during or after melting events.

395 The signs of metasomatism in the Khanka suite are scarce. It is dominated by peridotites
396 that show LREE-depleted pyroxene and bulk-rock compositions, and contain chemically
397 equilibrated minerals (Figs. 5 and 6; Plate 4, ES1) further indicating no significant addition
398 of metasomatic media after its formation by melt extraction. Only one xenolith has
399 LREE-enriched cpx. Rare, fine-grained interstitial materials and glass accompanied by
400 elevated K_2O and P_2O_5 and enrichments in La (Fig. 5a) in some WR samples may be linked
401 to the entrapment and transport of the xenoliths by host magmas. On the other hand, some
402 xenoliths show enrichments in U and Sr, elements that are highly incompatible and mobile
403 in hydrous fluids, not only in the WR but also in the cpx. These enrichments may have been
404 introduced to the Khanka CLM by low-volume fluids linked to subduction events, similar to
405 peridotites from island arcs that usually show enrichments in U and Sr and high U/Th (e.g.
406 Ionov, 2010).

407

408 *5.2 The age of the CLM in the Khanka block from Re-Os isotope data*

409 The Sviyagin peridotites display one of the best $^{187}\text{Os}/^{188}\text{Os}$ vs. $^{187}\text{Re}/^{188}\text{Os}$ correlations
410 reported as yet for a suite of mantle xenoliths (e.g. Rudnick and Walker, 2009). We attribute
411 this to the fact that these samples represent melting residues that have not been overprinted
412 by metasomatism. They appear to preserve relatively pristine Re-Os isotope systematics, not
413 disturbed significantly by Re mobility (Fig. 8) in the mantle after melting or during xenolith
414 transport, and therefore carry accurate age information on the CLM formation.

415 Though no statistically significant (with the sum of least squares less than 1) Re-Os
416 isochrons have been reported for any WR peridotite suites, the $^{187}\text{Os}/^{188}\text{Os}$ vs. $^{187}\text{Re}/^{188}\text{Os}$
417 correlations for a suite of peridotite xenoliths from Hannuoba in the mobile belt crosscutting
418 the North China craton (Gao et al., 2002) have been inferred to define robust CLM

419 formation ages (Liu et al., 2011; Rudnick and Walker, 2009). The eleven Hannuoba samples
420 reported by Gao et al. (2002) define nearly the same regression slope, hence apparent age, as
421 the twelve Sviyagin samples in this study and show similar scatter on the co-variation
422 diagram (Fig. 9a). Gao et al. (2012) argued that the Re-Os isotope systematics in at least one
423 Hannuoba xenolith had been disturbed, discarded three more samples plotting higher above
424 the correlation line and used a regression for seven samples forced through the present-day
425 PM composition to obtain an age of 1.91 ± 0.22 Ga. This value is identical to the Re-Os age
426 obtained without discarding any of the twelve Sviyagin xenoliths in this study and using our
427 preference of considering the data array *in toto*, as discussed above. Nonetheless, applying
428 an approach of Gao et al. (2012), i.e. consecutively disregarding Sviyagin samples with
429 highest deviations from $^{187}\text{Os}/^{188}\text{Os}$ vs. $^{187}\text{Re}/^{188}\text{Os}$ regression line, and forcing it through the
430 PM, yields ages from 1.8 to 2.3 Ga, depending on the selection of samples omitted from the
431 calculation. These age estimates are identical within the error margins, and consistent with
432 that from “alumina-chron” in Fig. 9b using $^{187}\text{Os}/^{188}\text{Os}$ value at 0.7 wt.% Al_2O_3 (e.g.
433 Rudnick and Walker, 2009).

434 There are many reasons why statistically valid Re-Os isochrons cannot be obtained for
435 mantle xenolith suites (e.g. Rudnick and Walker, 2009). Re-Os systematics in residual
436 peridotites may be perturbed by metasomatism, inadequately sampled due to the nugget
437 effect, modified during emplacement by contamination with relatively Re-rich host magmas,
438 and weathered near the surface. These factors, however, may be comparatively less
439 significant for the Sviyagin suite that shows no or little evidence for metasomatism (REE
440 patterns) or alteration (low LOI's). More important may be the random way that mantle
441 samples are picked up at depth. The xenoliths in this study come from a broad enough depth
442 range that they were too far apart to equilibrate with each other during melting or be formed
443 from a homogeneous source in a single melting episode. Rather, they likely formed in a
444 series of roughly coeval or successive episodes of melting of heterogeneous asthenosphere.
445 Overall, our data suggest that the CLM of the Khanka block formed in a Paleoproterozoic
446 tectonothermal event, but do not allow us to constrain its timing or duration more precisely
447 than the scatter on the Re-Os data array (Fig. 9a). But peridotite Re-Os age is important
448 because despite the fact that the crystalline basement of the Khanka block is not exposed in

449 Russia, detrital zircons from the southern Sikhote-Alin in the vicinity of the Khanka block
450 show a major ~1.8 Ga U-Pb age peak (e.g. [Liu et al., 2017a](#)), consistent with the
451 Paleoproterozoic (~1.9 Ga) age for the Khanka CLM in this study.

452

453 *5.3 Model age estimates of CLM formation*

454 Earlier studies ([Guo et al., 2017](#); [Wu et al., 2003](#); [Zhang et al., 2011, 2019](#)) attempted to
455 constrain the CLM formation age in NE China and the Khanka block using model Re-Os
456 (T_{MA}) or Re-depletion (T_{RD}) estimates ([Carlson, 2005](#); [Walker et al., 1989](#)) for individual
457 xenoliths. Such an approach, however, is questionable for off-craton peridotites. The lack of
458 ubiquitously high degrees of melt depletion, hence incomplete Re removal, usually means
459 that Os T_{RD} ages do not reflect true melt depletion ages ([Luguet and Reisberg, 2016](#); [Pearson](#)
460 [and Wittig, 2014](#)). This is why these studies ascribe an ancient T_{RD} age obtained for a single
461 sample, or a small number of most refractory samples, to the whole CLM domain, i.e.
462 assuming that the oldest model age of a given suite could be used to define the age of
463 melting. However, this can only be valid if the samples in the suite show a positive
464 $^{187}\text{Os}/^{188}\text{Os}$ vs. $^{187}\text{Re}/^{188}\text{Os}$ correlation, i.e. evidence for the formation in a single event from
465 a uniform source. By contrast, several lines of evidence suggest that the DMM, the
466 presumed source of the CLM, has a range of Os isotopic compositions, including rocks or
467 minerals with Proterozoic model ages ([Rudnick and Walker, 2009](#); [Walker, 2016](#)), that may
468 be older than true lithospheric formation ages of terrains in a given mobile belt ([Carlson and](#)
469 [Ionov, 2019](#)). Similarly uncertain, for comparable reasons, are age constraints in the
470 previous studies based exclusively on $^{187}\text{Os}/^{188}\text{Os}$ co-variation with melting indices
471 ([Reisberg and Lorand, 1995](#)) for the peridotite suites.

472 Sr-Nd isotope compositions of cpx from seven out of ten Sviyagin xenoliths shown in [Fig.](#)
473 [7](#) plot in the DMM field; many yield Proterozoic Rb-Sr (1.7–2.1 Ga) and Sm-Nd (1.0–1.6
474 Ga) model depletion ages relative to primitive mantle. Such estimates, however, are not
475 likely to reflect melting events during CLM formation. Even the most fertile (4.0–4.5 wt.%
476 Al_2O_3) unmetasomatized off-craton xenoliths, including those in the CAOB, may yield
477 similar Sr-Nd isotope values (e.g. [Ionov et al., 2005](#)), which appear to be typical of shallow
478 asthenosphere (e.g. [Carlson and Ionov, 2019](#)).

479 [Wang et al. \(2015\)](#) reported in situ Re-Os isotope data for interstitial sulfides in six
480 Sviyagin xenoliths, with T_{MA} ranging from negative values to 3.7 Ga, and T_{RD} from 0.23 to
481 1.66 Ga (mainly 0.7–1.2 Ga), as well as two much older values (2.6 and 2.8 Ga). These
482 values scatter broadly, may not be accurate, and likely record metasomatic rather than
483 melting events. However, [Wang et al. \(2015\)](#) used them to infer a Mesoproterozoic CLM
484 formation age, distinct from the Paleoproterozoic melting age obtained in this study.

485 We see at least three reasons why the WR Re-Os data in this study provide a better age
486 estimate than those reported by [Wang et al. \(2015\)](#). (1) Whole-rock analyses can be obtained
487 for any peridotites, not only those that contain sulfides, and therefore allow us to select the
488 best and most representative samples from the xenolith suite. In contrast, large sulfides are
489 required to obtain in-situ data on xenoliths. Therefore, samples analyzed by LA-ICPMS are,
490 by definition, biased to the very few rocks that have a specific type of metasomatism, which
491 introduces secondary sulfides. No large sulfides have been found in the xenoliths selected
492 for this study by optical inspection of thin sections. (2) WR data represent a much larger
493 volume of each xenolith, both in terms of the mass of the powder analyzed (1–2 g) and of
494 xenolith material crushed (>100 g) and ground to powder (>20 g). Therefore, the WR data
495 are based on a more representative sampling that includes large numbers of Os-hosting
496 grains rather than the one advantageous grain that can be analyzed by LA-ICPMS. (3) Age
497 estimates in this study are based on an array of $^{187}\text{Os}/^{188}\text{Os}$ vs. $^{187}\text{Re}/^{188}\text{Os}$ data for 18
498 xenoliths from two independent studies compared to model ages for individual sulfide grains
499 from six xenoliths. This array also has an initial $^{187}\text{Os}/^{188}\text{Os}$ of ~0.116 that supports the
500 formation of this block of CLM from the convecting mantle around 2 Ga.

501 Generally, the robustness, accuracy and relevance of the lithospheric formation age
502 estimates from individual in-situ sulfide analyses by LA-ICPMS are doubtful, in particular
503 for interstitial sulfides in off-craton peridotites ([Pearson et al., 2014](#); [Rudnick and Walker,](#)
504 [2009](#)). The dominant Os hosts in pristine refractory peridotites are Os-Ir alloys. Sulfides are
505 some of the first phases to enter the melt during melting even below the peridotite solidus,
506 hence they are most likely metasomatic in nature in xenoliths ([Lorand and Grégoire, 2006](#);
507 [Reisberg et al., 2005](#)), in particular those sufficiently large for in situ analyses and, by
508 definition, carry a mixed and uncertain Os isotope signal.

509

510 *5.4 Khanka peridotites compared with those in North China and CAOB*

511 It is relevant to compare mantle xenoliths from the Khanka block with those from the
512 adjacent North China in general and the eastern CAOB in particular. The Khanka peridotites
513 may have much in common with those from Hannuoba in the Trans-North China Orogen, at
514 the northern margin of the North China Craton (NCC) (Rudnick et al., 2004) where cratonic
515 CLM was replaced by juvenile material in the Paleoproterozoic. The Khanka and Hannuoba
516 peridotites have similar modal, major element, Os and Sr-Nd isotope ranges and age (Fig. 9).
517 On the other hand, the Hannuoba xenoliths show common LREE-enrichments, have
518 abundant, coarse sulfides and high S abundances as well as nearly flat, PM-like HSE
519 patterns (Gao et al., 2002; Liu et al., 2011). Little, if any, compositional distinction has been
520 found between the CLM of the NCC replaced in the Paleoproterozoic (Hannuoba) and in the
521 Phanerozoic (Qixia) (Rudnick et al., 2004).

522 Mantle xenoliths have been reported from several locations in NE China east and
523 southeast of the Khanka block: Shuangliao, Yitong, Jiaohe and Wangqing in the eastern
524 CAOB (Wu et al., 2003; Yu et al., 2009), Nuomin and Keluo in the Xingan block of the
525 CAOB as well as Huinan and Kuandian in the NE NCC (Fig. 1). In general, these sites have
526 more diverse xenolith types than in the Khanka block with harzburgites (Fig. 2), wehrlites
527 and pyroxenites being more common. The peridotites at each site in the eastern CAOB are
528 generally more refractory (averages: 1.9–2.4 wt.% Al₂O₃, 1.6–2.4 wt.% CaO, 40–43 wt.%
529 MgO) than in the Khanka block (Plate 3, ES1).

530 The majority of the Kelou xenoliths (Zhang et al., 2011) are metasomatized dunites,
531 harzburgites and low-cpx lherzolites. Zhang et al. (2011) interpreted a highly scattered
532 “alumino-chron” and ancient (~2 Ga) T_{RD} ages for three refractory rocks as representing
533 CLM formation ages decoupled from crustal ages. They also inferred unrealistically low
534 melt extraction degrees (3–11%) for the harzburgites owing to erroneous trace element
535 modeling. The nearby Nuomin xenolith suite (Zhang et al., 2019) is dominated by refractory
536 peridotites as well. Zhang et al. (2019) report a broad range of T_{RD} ages (0.5–1.6 Ga) for
537 these rocks, yet interpret them as fragments of coexisting Paleo-Mesoproterozoic and
538 Neoproterozoic CLM in the region, contrary to the evident fallacy of using single T_{RD}

539 estimates for individual off-craton xenoliths as CLM formation ages that represent a mantle
540 portion (Rudnick and Walker, 2009; Walker, 2016). By comparison, xenoliths from Tariat in
541 central Mongolia define an excellent “alumino-chron”, but show no $^{187}\text{Os}/^{188}\text{Os}$ vs.
542 $^{187}\text{Re}/^{188}\text{Os}$ correlation, which led Carlson and Ionov (2019) to interpret them as essentially
543 undifferentiated MORB-source mantle that was accreted during the ocean-closing events
544 that formed the CAOB.

545 The peridotites from Huinan (Xu et al., 2003) and Kuandian (Wu et al., 2006) in the NE
546 NCC and some other sites have much higher FeO than experimental melting residues of
547 fertile mantle (Plate 3, ES1; Herzberg, 2004), most likely due to reaction with Fe-enriched
548 melts that may ultimately produce wehrlites (Ionov et al., 2005) or opx-rich peridotites (Xu
549 et al., 2003), depending on melt compositions. As a result, the NE China peridotites tend to
550 have higher FeO and lower Mg# and SiO_2 than the Khanka peridotites at similar Al_2O_3
551 (Plates 3–4, ES1), and also show a broader HREE range with mainly LREE-enriched REE
552 patterns (Plate 6, ES1). This contrasts with the mainly LREE-depleted Khanka CLM.

553 Overall, the Khanka mantle xenoliths in this study are distinct in modal and chemical
554 compositions from those in nearby localities in the eastern CAOB in NE China (Fig. 1). The
555 Khanka CLM is dominated by moderately depleted lherzolites that are mostly unaffected by
556 metasomatism and in this regard are more similar to xenolith suites in central Mongolia
557 (Ionov, 2002, 2007; Carlson and Ionov, 2019) and southern Siberia (Ionov et al., 2005) to the
558 west in the CAOB. This contrasts with higher proportions of harzburgites and other rocks
559 (wehrlite, pyroxenite) overprinted by metasomatism, commonly attributed to subduction, in
560 nearby NE China (eastern CAOB and the NE NCC) where the cratonic CLM was replaced
561 or reworked in the Meso-Cenozoic.

562

563 *5.5 The age and composition of CLM in orogenic belts*

564 The CLM in orogenic belts may have a complex structure with a range of compositions
565 and ages. One reason for this complexity is the varied nature of lithospheric components
566 assembled in the belts, from island arcs and other oceanic domains with juvenile lithosphere
567 to ancient continental fragments (micro-continents) (e.g. Zhou et al., 2018). The late
568 Paleozoic to early Mesozoic subduction zones where the CAOB components were

569 assembled are located in central and southern Mongolia and NE China (e.g. [Wilde, 2015](#))
570 away from the North China Craton (NCC). Therefore, though southern CAOB borders on
571 the NCC now, it was not built against or around it, and therefore is not likely to incorporate
572 remobilized Archean CLM components.

573 Another reason for its complex structure is the potentially variable influence of
574 subduction processes on these CLM domains during and after the closure of oceanic basins
575 (e.g. [Ionov et al., 2017](#); [Liu et al., 2011](#)). A fundamental question regarding the CLM in
576 orogenic belts is whether it is expansively re-worked by the subduction-related
577 metasomatism, or alternatively, the re-working is spatially limited.

578 The subduction of the Paleo-Asian and Pacific slabs has significantly influenced the
579 lithospheric architecture of eastern China, including the destruction of the CLM in eastern
580 NCC ([Zhu et al., 2012](#)), the formation of the Songliao basin in the easternmost CAOB ([Liu
581 et al., 2017b](#)), and metasomatism in mantle xenoliths, either directly by slab-derived melts
582 and fluids ([Deng et al., 2017](#)) or via related asthenospheric upwelling ([Guo et al., 2017](#)).
583 Overall, literature data on basalt-hosted mantle xenoliths in NE China seems to suggest
584 widespread and intense CLM re-working by metasomatism, though specific links between
585 the subduction and CLM modification continue to be debated.

586 By comparison, the results in this study demonstrate for the first time that the CLM of
587 the Khanka block, i.e. the nearest CAOB segment to the Asian Pacific margin, shows no or
588 very limited metasomatic effects. Moreover, it retains chemical and isotopic signatures of its
589 formation by melt extraction at ~2 Ga including Re-Os isotope relations. It follows that the
590 CLM re-working in orogenic belts, both in the CAOB and worldwide, is not widespread and
591 may be limited to weaker lithospheric portions that also concentrate basaltic magmatism. In
592 this regard, the Khanka CLM resembles that in the Tariat region of central Mongolia in the
593 central CAOB ([Carlson and Ionov, 2019](#)), which is composed mainly by very fertile
594 lherzolites and thus is distinct from CLM typical of subduction zones ([Arai et al., 2007](#);
595 [Ionov, 2010](#)).

596 The factors determining the strength and stability of the CLM remain poorly constrained.
597 The findings in this study suggest that relatively fertile, pyroxene-rich CLM domains may
598 be more resistant to widespread metasomatic reworking, and ultimately to destruction, than

599 refractory, olivine-rich CLM. This may be related to better permeability of olivine-rich
600 rocks to carbonatite as well as silicate metasomatic media (e.g. [Ionov et al., 2006a](#)).

601 The reason for the high proportion of metasomatized rocks among mantle xenoliths at
602 some North China sites may be CLM reaction with source liquids of young mafic magmas
603 that carry the xenoliths. If such sub-lithospheric liquids stall and fractionate in the lower
604 CLM before the eruption, they will affect the host mantle. The situation may be similar to
605 the high proportion (~60%) of sheared and metasomatized (Fe-Ti-rich) garnet peridotites
606 among kimberlite-hosted xenoliths in the SE ([Ionov et al., 2005, 2006a](#)) and central Siberian
607 craton ([Agashev et al., 2013; Doucet et al., 2013](#)). Chemical and geophysical modeling link
608 the deformation and metasomatism in cratonic roots with kimberlite-related fluids, and
609 demonstrate that the CLM with a high share of Fe-rich peridotites cannot be rheologically
610 stable and long-living ([Bascou et al., 2011; Doucet et al., 2014](#)).

611

612 **6. Summary of conclusions**

613 The mantle xenoliths hosted by Cenozoic basalts in the Precambrian Khanka block in
614 far eastern Russia between NE China and the Pacific coast of Asia, provide insights into the
615 CLM of the eastern CAOB and other off-craton orogenic belts. The modal and chemical data
616 suggest that the Khanka peridotites are residues of low to moderate degrees of melt
617 extraction from fertile mantle with no or limited effects of metasomatism in spite of the
618 proximity to subduction zones in the Pacific. This contrasts with the pervasive metasomatic
619 reworking of the CLM beneath many adjacent regions, including NE China (e.g. [Deng et al.,
2017; Yu et al., 2009](#)), SE Siberian craton ([Ionov et al., 2006c](#)) and the localities closer to the
621 Pacific coast in far eastern Russia ([Ionov et al., 1999; Ionov et al., 1995](#)). The Sviyagin
622 peridotites display one of the best $^{187}\text{Os}/^{188}\text{Os}$ vs. $^{187}\text{Re}/^{188}\text{Os}$ correlations reported for a
623 mantle xenolith suite and provide the first robust CLM age constraint for the eastern CAOB.
624 The Paleoproterozoic CLM of the Khanka block, with LREE-depleted cpx and Sr-Nd
625 isotope ratios typical of the MORB mantle, persisted through Phanerozoic orogenies, unlike
626 most of mantle xenoliths reported from nearby NE China. This study suggests that
627 melt-depleted, but relatively fertile Proterozoic CLM domains in orogenic belts may not be
628 expansively re-worked during the closure of ocean basins and collision events, and may be

629 tectonically resilient.

630

631 **Acknowledgements**

632 DAI thanks V. Prikhodko for guidance with fieldwork and acknowledges support from
633 the Max-Planck-Institute (Mainz, Germany) in 2003-2005, and Chinese Academy of
634 Sciences President's International Fellowship Initiative (PIFI) for Visiting Scientists in 2017
635 and in 2019 (Grant No. 2017VCA0009). PG acknowledges a fellowship from China
636 Scholarship Council as a joint PhD student at the Montpellier University, France as well as
637 financial support from the National Natural Science Foundation of China (Grant 91858211)
638 and National Key Research and Development Project (2017YFC0601304).

639

640 **Figure Captions**

641 **Fig. 1.** A sketch map of NE China and southern far eastern Russia showing the tectonic
642 framework, major areas of Cenozoic basaltic volcanism (grey fields) and mantle xenolith
643 occurrences (stars). CAOB: Central Asian Orogenic Belt including its major tectonic units
644 (blocks, massifs) in NE China: Erguna, Xing'an, Songnen, Jiamusi-Bureya and Khanka. The
645 xenoliths in this study are from Sviyagin and Podgelban in the Khanka block.

646 **Fig. 2.** Modal compositions of peridotite xenoliths from the Khanka block in this study
647 (filled circles) and those reported by [Guo et al. \(2017\)](#) (open circles) in comparison with
648 peridotite xenoliths from the CAOB in NE China ([Xu et al., 1998](#); [Yu et al., 2009](#)) as well as
649 references on Chinese localities (grey squares) provided in ES1.

650 **Fig. 3.** Plots of Al_2O_3 vs. major oxide and Yb concentrations and Mg# (molar
651 $\text{Mg}/(\text{Mg}+\text{Fe})$) for whole-rock (WR) peridotite xenoliths from Khanka in this study (large
652 filled circles) and those reported by [Guo et al. \(2017\)](#) (open circles). Also shown are
653 primitive mantle (PM [McDonough and Sun, 1995](#)) and peridotite xenoliths from central
654 CAOB (Tariat in Mongolia, small grey circles) that experienced melt extraction ([Ionov, 2007](#);
655 [Ionov and Hofmann, 2007](#)); the latter overlap the Khanka suite at moderate Al_2O_3 (melt
656 depletion degrees) and extend the melting-related trends to the PM. Grey dashed lines are
657 correlation trends (exponential trends show best fits for Na_2O and TiO_2), r^2 are correlation
658 coefficients. Blue dotted lines in (a) show isobaric batch melting residues of fertile mantle at

659 1, 2, 3 and 4 GPa, continuous red lines are residues of polybaric fractional melting at 2–0, 3–
660 0, 5–1 and 7–2 GPa (Herzberg, 2004). See online version for color code.

661 **Fig. 4.** Co-variation plots for Al₂O₃, Mg# (molar Mg/(Mg+Fe)) and modal cpx in WR
662 xenoliths, Mg# in olivine and Cr# (molar Cr/(Cr+Al)) in spinel for xenoliths in this study
663 and from Guo et al. (2017). Shown for comparison are peridotite xenoliths from central
664 CAOB (Tariat in Mongolia, small grey circles) dominated by fertile spinel lherzolites (Ionov,
665 2007; Ionov and Hofmann, 2007). Exponential correlation trends (dashed grey lines) show
666 best fits for plots of Cr#_{sp}, r² are correlation coefficients.

667 **Fig. 5.** Rare earth element (REE, left) and lithophile trace element (right) patterns for WR
668 xenoliths (top) and clinopyroxenes (cpx, bottom) in this study normalized to primitive
669 mantle (PM) (McDonough and Sun, 1995). The cpx patterns for all samples except Sv-17
670 show regular, continuous depletion from heavy and medium to light REE; cpx and WR
671 Sv-17 is enriched in light REE. Xenolith Sv-32 has the lowest medium and heavy REE in
672 the cpx (c) and WR (a) as well as the lowest modal cpx and Al₂O₃ (Fig. 4d). WR patterns (b)
673 show common positive anomalies for U, Sr and Ba likely due to fluid metasomatism.

674 **Fig. 6.** PM-normalized (McDonough and Sun, 1995) REE (a) and lithophile trace element
675 (b) patterns for orthopyroxene (opx), and the cpx/opx concentration ratios for the REE (c)
676 and lithophile trace elements (d). The opx patterns in (a) show continuous, steep trends of
677 depletion in less compatible REE. The cpx/opx show a coherent and narrow range for all but
678 the most incompatible elements suggesting chemical equilibration of minerals in the rocks.

679 **Fig. 7.** Plots of ⁸⁷Sr/⁸⁶Sr vs. ¹⁴³Nd/¹⁴⁴Nd for clinopyroxene in xenoliths in this study (large
680 circles), cpx reported by Nishio et al. (2004) (small grey circles) and a host Sviyagin basalt.
681 Also shown are mantle end-members and fields for oceanic basalts (Zindler and Hart, 1986),
682 as well as literature data for peridotite xenoliths (Xu et al., 1998; Yu et al., 2009) and basalts
683 (Kuritani et al., 2011; Xu et al., 2012) from NE China.

684 **Fig. 8.** Patterns for PGE and Re in WR xenoliths in this study normalized to primitive
685 upper mantle (Becker et al., 2006). Coherent, continuous depletion from Ir to Re indicates
686 melt extraction and no significant post-melting metasomatism. Low Os/Ir ratios are common
687 in basalt-hosted, off-craton mantle xenoliths (see text for discussion).

688 **Fig. 9.** ¹⁸⁷Os/¹⁸⁸Os plotted vs. ¹⁸⁷Re/¹⁸⁸Os (a), Al₂O₃ (b), CaO (c) and MgO (d) for WR

689 xenoliths in this study (large circles); black lines are linear correlation trends, r^2 are
690 correlation coefficients for the datasets. The equation in the $^{187}\text{Os}/^{188}\text{Os}$ vs. $^{187}\text{Re}/^{188}\text{Os}$
691 diagram (a) shows the slope (implying an 1.9 Ga age) and the initial for the linear regression
692 through all the samples in this study (grey area). Also shown are PUM (Meisel et al., 2001),
693 Sviyagin xenoliths from Guo et al. (2017) (small open circles) and (a-b) peridotite xenoliths
694 from Hannuoba in North China craton (Gao et al., 2002) (crosses); the dotted line in (a)
695 shows the regression for all the Hannuoba xenoliths, which has about the same slope (i.e.
696 defining the same age) as for the Sviyagin suite.

697

698

Supplemental Materials

699

Electronic supplement 1 (ES1): Supplementary figures

700

Plate 1: Sampling site, basaltic outcrops and xenolith occurrences near Sviyagino.

701

Plate 2: Photomicrographs of representative Sviyagin spinel peridotite xenoliths.

702

Plate 3: Major oxides vs. Al_2O_3 vs. for peridotite xenoliths from this study and NE China.

703

Plate 4. $\text{Mg}\#_{\text{WR}}$ vs. $\text{Mg}\#_{\text{O1}}$ for peridotite xenoliths in this study and from NE China.

704

Plate 5. MREE-HREE WR patterns for xenoliths in this study and melting modeling.

705

Plate 6. PM-normalized REE patterns for WR peridotite xenoliths from NE China.

706

707

Electronic supplement 2 (ES2): Methods

708

709

Electronic supplement 3 (ES3): Analytical results

710

Table 1: Major elements in whole-rock (WR) samples from XRF analyses.

711

Table 2: Major elements in minerals by EPMA.

712

Table 3: Trace elements analyses of WR by LA-ICPMS of fused WR powders.

713

Table 4: Trace element analyses of pyroxenes by LA-ICPMS.

714

Table 5: Sr-Nd isotope analyses of clinopyroxenes by TIMS.

715

Table 6: PGE and Re concentrations and Os isotope analyses of WR xenoliths.

716

717

References

718

Agashev A.M., Ionov D.A, Pokhilenko NP, Golovin AV, Cherepanova Yu.V, Sharygin I.S. (2013)

719 Metasomatism in lithospheric mantle roots: constraints from whole-rock and mineral chemical
720 composition of deformed peridotite xenoliths from kimberlite pipe Udachnaya. *Lithos* 160-161,
721 201-215.

722 Arai, S., Abe, N. and Ishimaru, S. (2007) Mantle peridotites from the Western Pacific. *Gondwana*
723 *Research* 11, 180-199.

724 Bascou J., Doucet L.S., Saumet S., Ionov D.A., Ashchepkov I.V., Golovin A.V. (2011) Seismic
725 velocities, anisotropy and deformation in Siberian cratonic mantle: EBSD data on xenoliths from the
726 Udachnaya kimberlite. *Earth Planet. Sci. Lett.* 304, 71-84.

727 Becker, H., Horan, M.F., Walker, R.J., Gao, S., Lorand, J.P. and Rudnick, R.L. (2006) Highly
728 siderophile element composition of the Earth's primitive upper mantle: Constraints from new data on
729 peridotite massifs and xenoliths. *Geochimica et Cosmochimica Acta* 70, 4528-4550.

730 Carlson, R.W. (2005) Application of the Pt–Re–Os isotopic systems to mantle geochemistry and
731 geochronology. *Lithos* 82, 249-272.

732 Carlson, R.W. and Ionov, D.A. (2019) Compositional characteristics of the MORB mantle and
733 bulk silicate earth based on spinel peridotites from the Tariat Region, Mongolia. *Geochimica et*
734 *Cosmochimica Acta* 257, 206-223.

735 Cohen, A.S. and Waters, F.G. (1996) Separation of osmium from geological materials by solvent
736 extraction for analysis by thermal ionisation mass spectrometry, *Analytica Chimica Acta*, 332,
737 269-275.

738 Deng, L., Liu, Y., Zong, K., Zhu, L., Xu, R., Hu, Z. and Gao, S. (2017) Trace element and Sr
739 isotope records of multi-episode carbonatite metasomatism on the eastern margin of the North China
740 Craton. *Geochemistry, Geophysics, Geosystems* 18, 220-237.

741 Doucet L.S., Peslier A.H., Ionov D.A., Brandon A.D., Golovin A.V., Goncharov A.G.,
742 Ashchepkov I.V. (2014) High water contents in the Siberian cratonic mantle linked to metasomatism:
743 an FTIR study of Udachnaya peridotite xenoliths. *Geochim. Cosmochim. Acta* 137, 159-187.

744 Doucet L.S., Ionov D.A., Golovin A.V. (2013) The origin of coarse garnet peridotites in cratonic
745 lithosphere: new data on xenoliths from the Udachnaya kimberlite, central Siberia. *Contrib. Miner.*
746 *Petrol.* 165, 1225-1242

747 Gao, S., Rudnick, R.L., Carlson, R.W., McDonough, W.F. and Liu, Y.-S. (2002) Re-Os evidence
748 for replacement of ancient mantle lithosphere beneath the North China craton. *Earth Planet Sci Lett*
749 198, 307-322.

750 Guo, P., Xu, W.-L., Wang, C.-G., Wang, F., Ge, W.-C., Sorokin, A.A. and Wang, Z.-W. (2017)
751 Age and evolution of the lithospheric mantle beneath the Khanka Massif: Geochemical and Re–Os
752 isotopic evidence from Sviyagino mantle xenoliths. *Lithos* 282–283, 326-338.

753 Herzberg, C. (2004) Geodynamic information in peridotite petrology. *Journal of Petrology* 45,
754 2507-2530.

755 Ionov, D. (2002) Mantle structure and rifting processes in the Baikal-Mongolia region:
756 geophysical data and evidence from xenoliths in volcanic rocks. *Tectonophysics* 351, 41-60.

757 Ionov, D.A. (2007) Compositional variations and heterogeneity in fertile lithospheric mantle:
758 peridotite xenoliths in basalts from Tariat, Mongolia. *Contrib. Mineral. Petrol.* 154, 455-477.

759 Ionov, D.A. (2010) Petrology of mantle wedge lithosphere: New data on supra-subduction zone
760 peridotite xenoliths from the andesitic Avacha volcano, Kamchatka. *Journal of Petrology* 51,
761 327-361.

762 Ionov, D.A., Ashchepkov, I. and Jagoutz, E. (2005). The provenance of fertile off-craton

763 lithospheric mantle: Sr-Nd isotope and chemical composition of garnet and spinel peridotite
764 xenoliths from Vitim, Siberia. *Chemical Geology* 217, 41-75.

765 Ionov, D.A., Bigot, F. and Braga, R. (2017) The Provenance of the Lithospheric Mantle in
766 Continental Collision Zones: Petrology and Geochemistry of Peridotites in the Ulten–Nonsberg Zone
767 (Eastern Alps). *Journal of Petrology* 58, 1451-1472.

768 Ionov, D.A., Chanefo, I. and Bodinier, J.-L. (2005) Origin of Fe-rich lherzolites and wehrlites
769 from Tok, SE Siberia by reactive melt percolation in refractory mantle peridotites. *Contributions to
770 Mineralogy and Petrology* 150, 335-353.

771 Ionov, D.A., Chazot, G., Chauvel, C., Merlet, C. and Bodinier, J.-L. (2006a) Trace element
772 distribution in peridotite xenoliths from Tok, SE Siberian craton: A record of pervasive, multi-stage
773 metasomatism in shallow refractory mantle. *Geochimica et Cosmochimica Acta* 70, 1231-1260.

774 Ionov, D.A., Doucet, L.S., Carlson, R.W., Golovin, A.V. and Korsakov, A.V. (2015) Post-Archean
775 formation of the lithospheric mantle in the central Siberian craton: Re–Os and PGE study of
776 peridotite xenoliths from the Udachnaya kimberlite. *Geochimica et Cosmochimica Acta* 165,
777 466-483.

778 Ionov DA, Doucet LS, Pogge von Strandmann PAE, Golovin AV, Korsakov AV (2017) Links
779 between deformation, chemical enrichments and Li-isotope compositions in the lithospheric mantle
780 of the central Siberian craton. *Chem. Geol.* 475, 105-121,

781 Ionov, D.A., Grégoire, M. and Prikhod'ko, V.S. (1999) Feldspar-Ti-oxide metasomatism in
782 off-cratonic continental and oceanic upper mantle. *Earth and Planetary Science Letters* 165, 37-44.

783 Ionov, D.A. and Hofmann, A.W. (2007) Depth of formation of sub-continental off-craton
784 peridotites. *Earth and Planetary Science Letters* 261, 620-634.

785 Ionov, D.A., Hofmann, A.W., Merlet, C., Gurenko, A.A., Hellebrand, E., Montagnac, G., Gillet, P.
786 and Prikhodko, V.S. (2006b) Discovery of whitlockite in mantle xenoliths: Inferences for water- and
787 halogen-poor fluids and trace element residence in the terrestrial upper mantle. *Earth and Planetary
788 Science Letters* 244, 201-217.

789 Ionov, D.A., Prikhodko, V.S. and O'Reilly, S.Y. (1995) Peridotite xenoliths in alkali basalts from
790 the Sikhote-Alin, southeastern Siberia, Russia: trace element signatures of mantle beneath a
791 convergent continental margin. *Chem Geol* 120, 275-294.

792 Ionov, D.A., Shirey, S.B., Weis, D. and Brüggmann, G. (2006c) Os-Hf-Sr-Nd isotope and PGE
793 systematics of spinel peridotite xenoliths from Tok, SE Siberian craton: Effects of pervasive
794 metasomatism in shallow refractory mantle. *Earth and Planetary Science Letters* 241, 47-64.

795 Kalfoun, F., Ionov, D. and Merlet, C. (2002) HFSE residence and Nb-Ta ratios in metasomatised,
796 rutile-bearing mantle peridotites. *Earth and Planetary Science Letters* 199, 49-65.

797 Kuritani, T., Ohtani, E. and Kimura, J.-I. (2011) Intensive hydration of the mantle transition zone
798 beneath China caused by ancient slab stagnation. *Nature Geosci* 4, 713-716.

799 Liu, J., Cai, R., Pearson, D.G., Scott, J.M., 2019. Thinning and destruction of the lithospheric
800 mantle root beneath the North China Craton: A review. *Earth-Science Reviews* 196, 102873.

801 Liu, J., Rudnick, R.L., Walker, R.J., Gao, S., Wu, F.-y., Piccoli, P.M., Yuan, H., Xu, W.-l. and Xu,
802 Y.-G. (2011) Mapping lithospheric boundaries using Os isotopes of mantle xenoliths: An example
803 from the North China Craton. *Geochimica et Cosmochimica Acta* 75, 3881-3902.

804 Liu, K., Zhang, J., Wilde, S.A., Liu, S., Guo, F., Kasatkin, S.A., Golozoubov, V.V., Ge, M., Wang,
805 M. and Wang, J. (2017a) U-Pb dating and Lu-Hf isotopes of detrital zircons from the southern
806 Sikhote-Alin orogenic belt, Russian Far East: Tectonic implications for the Early Cretaceous

807 evolution of the Northwest Pacific margin. *Tectonics* 36, 2555–2598.

808 Liu, Y., Li, W., Feng, Z., Wen, Q., Neubauer, F. and Liang, C. (2017b) A review of the Paleozoic
809 tectonics in the eastern part of Central Asian Orogenic Belt. *Gondwana Research* 43, 123-148.

810 Lorand, J.-P. and Grégoire, M. (2006) Petrogenesis of base metal sulphide assemblages of some
811 peridotites from the Kaapvaal craton (South Africa). *Contrib. Mineral. Petrol.* 151, 521-538.

812 Luguet, A. and Reisberg, L. (2016) Highly Siderophile Element and ^{187}Os Signatures in
813 Non-cratonic Basalt-hosted Peridotite Xenoliths: Unravelling the Origin and Evolution of the
814 Post-Archean Lithospheric Mantle. *Reviews in Mineralogy & Geochemistry* 81, 305-368.

815 McDonough, W.F. and Sun, S.-s. (1995) The composition of the Earth. *Chem Geol* 120, 223-253.

816 Meisel, T., Walker, R.J., Irving, A.J. and Lorand, J.-P. (2001) Osmium isotopic compositions of
817 mantle xenoliths: a global perspective. *Geochim. Cosmochim. Acta* 65, 1311-1323.

818 Menzies, M.A., Fan, W. and Zhang, M. (1993) Paleozoic and Cenozoic lithoprobes and the loss
819 of >120 km of Archaean lithosphere, Sino-Korean craton. *Geol. Soc. London Spec. Publ.* 76, 71-81.

820 Nishio, Y., Nakai, S., Yamamoto, J., Sumino, H., Matsumoto, T., Prikhod'ko, V.S. and Arai, S.
821 (2004) Lithium isotopic systematics of the mantle-derived ultramafic xenoliths: implications for
822 EM1 origin. *Earth Planet Sci Lett* 217, 245-261.

823 Okamura, S., Arculus, R.J. and Martynov, Y.A. (2005) Cenozoic Magmatism of the North-Eastern
824 Eurasian Margin: The Role of Lithosphere Versus Asthenosphere. *J. Petrol.* 46, 221-253.

825 Okamura, S., Martynov, Y.A., Furuyama, K. and Nagao, K. (1998) K-Ar ages of the basaltic
826 rocks from far east Russia: Constraints on the tectono-magmatism associated with the Japan Sea
827 opening. *The Island Arc* 7, 271-282.

828 Pearson, D.G., Canil, D. and Shirey, S.B. (2014) Mantle samples included in volcanic rocks:
829 Xenoliths and diamonds, in: Carlson, R.W. (Ed.), *Treatise on Geochemistry (Second Edition)*.
830 Elsevier, Oxford, pp. 169-253.

831 Pearson, D.G., Irvine, G.J., Ionov, D.A., Boyd, F.R. and Dreibus, G.E. (2004) Re-Os isotope
832 systematics and platinum group element fractionation during mantle melt extraction: a study of
833 massif and xenolith peridotite suites. *Chem Geol* 208, 29-59.

834 Pearson, D.G. and Wittig, N. (2014) The Formation and Evolution of Cratonic Mantle
835 Lithosphere – Evidence from Mantle Xenoliths, *Treatise on Geochemistry (Second Edition)*. Elsevier,
836 Oxford, pp. 255-292.

837 Reisberg, L. and Lorand, J.P. (1995) Longevity of sub-continental mantle lithosphere from
838 osmium isotope systematics in orogenic peridotite massifs. *Nature* 376, 159-162.
839 286-308.

840 Reisberg, L., Zhi, X., Lorand, J.-P., Wagner, C., Peng, Z. and Zimmermann, C. (2005). Re–Os and
841 S systematics of spinel peridotite xenoliths from east central China: Evidence for contrasting effects
842 of melt percolation. *Earth Planet Sci Lett* 239, 286-308.

843 Rudnick, R.L., Gao, S., Ling, W.-l., Liu, Y.-s. and McDonough, W.F. (2004) Petrology and
844 geochemistry of spinel peridotite xenoliths from Hannuoba and Qixia, North China craton. *Lithos* 77,
845 609-637.

846 Rudnick, R.L. and Walker, R.J. (2009) Interpreting ages from Re–Os isotopes in peridotites
847 *Lithos* 112, Supplement 2, 1083-1095.

848 Takazawa, E., Frey, F.A., Shimizu, N. and Obata, M. (2000) Whole rock compositional variations
849 in an upper mantle peridotite (Horoman, Hokkaido, Japan): Are they consistent with a partial melting
850 process. *Geochimica et Cosmochimica Acta* 64, 695-716.

851 Walker, R.J. (2016) Siderophile Elements in Tracing Planetary Formation and Evolution.
852 *Geochemical Perspectives* 5, 1-145.

853 Walker, R.J., Carlson, R.W., Shirey, S.B. and Boyd, F.R. (1989) Os, Sr, Nd, and Pb isotope
854 systematics of southern African peridotite xenoliths: Implications for the chemical evolution of
855 subcontinental mantle. *Geochim. Cosmochim. Acta* 53, 1583-1595.

856 Wang, K.-L., Prikhodko, V., O'Reilly, S.Y., Griffin, W.L., Pearson, N.J., Kovach, V., Iizuka, Y.
857 and Chien, Y.-H. (2015) Ancient mantle lithosphere beneath the Khanka massif in the Russian Far
858 East: in situ Re-Os evidence. *Terra Nova* 27, 277-284.

859 Wilde, S.A. (2015) Final amalgamation of the Central Asian Orogenic Belt in NE China:
860 Paleo-Asian Ocean closure versus Paleo-Pacific plate subduction — A review of the evidence.
861 *Tectonophysics* 662, 345-362.

862 Wu, F.-y., Walker, R.J., Ren, X.-w., Sun, D.-y. and Zhou, X.-h. (2003) Osmium isotopic
863 constraints on the age of lithospheric mantle beneath northeastern China. *Chem Geol* 196, 107-129.

864 Wu, F.-Y., Walker, R.J., Yang, Y.-H., Yuan, H.-L. and Yang, J.-H. (2006) The chemical-temporal
865 evolution of lithospheric mantle underlying the North China Craton. *Geochimica et Cosmochimica*
866 *Acta* 70, 5013-5034.

867 Xu, B., Zhao, P., Wang, Y., Liao, W., Luo, Z., Bao, Q. and Zhou, Y. (2015) The pre-Devonian
868 tectonic framework of Xing'an–Mongolia orogenic belt (XMOB) in north China. *Journal of Asian*
869 *Earth Sciences* 97, 183-196.

870 Xu, Y., Menzies, M.A., Vroon, P., Mercier, J.-C. and Lin, C. (1998)
871 Texture-temperature-geochemistry relationships in the upper mantle as revealed from spinel
872 peridotite xenoliths from Wangqing, NE China. *J. Petrol.* 39, 469-493.

873 Xu, Y.-G. (2014) Recycled oceanic crust in the source of 90–40Ma basalts in North and Northeast
874 China: Evidence, provenance and significance. *Geochimica et Cosmochimica Acta* 143, 49-67.

875 Xu, Y.-G., Menzies, M.A., Thirlwall, M.F., Huang, X.-L., Liu, Y. and Chen, X.-M. (2003)
876 "Reactive" harzburgites from Huinan, NE China: products of the lithosphere-asthenosphere
877 interaction during lithospheric thinning? *Geochim. Cosmochim. Acta* 67, 487-505.

878 Xu, Y.-G., Zhang, H.-H., Qiu, H.-N., Ge, W.-C. and Wu, F.-Y. (2012) Oceanic crust components
879 in continental basalts from Shuangliao, Northeast China: Derived from the mantle transition zone?
880 *Chem Geol* 328, 168-184.

881 Xu, Y.G., Mercier, J.-C.C., Menzies, M.A., Ross, J.V., Harte, B., Lin, C. and Shi, L. (1996) K-rich
882 glass-bearing wehrlite xenoliths from Yitong, northeastern China: petrological and chemical
883 evidence for mantle metasomatism. *Contrib. Mineral. Petrol.* 125, 406-420.

884 Yu, S.-Y., Xu, Y.-G., Huang, X.-L., Ma, J.-L., Ge, W.-C., Zhang, H.-H. and Qin, X.-F. (2009)
885 Hf-Nd isotopic decoupling in continental mantle lithosphere beneath Northeast China: Effects of
886 pervasive mantle metasomatism. *Journal of Asian Earth Sciences* 35, 554-570.

887 Zhang, Y.-L., Liu, C.-Z., Ge, W.-C., Wu, F.-Y. and Chu, Z.-Y. (2011) Ancient sub-continental
888 lithospheric mantle (SCLM) beneath the eastern part of the Central Asian Orogenic Belt (CAOB):
889 Implications for crust-mantle decoupling. *Lithos* 126, 233-247.

890 Zhang, Y.-L., Ge, W.C., Sun, J., Yang, H., Liu, Z.C., Liu, J.G., 2019. Age and composition of the
891 subcontinental lithospheric mantle beneath the Xing'an-Mongolia Orogenic Belt: Implications for the
892 construction of microcontinents during accretionary orogenesis. *Lithos* 326, 556-571.

893 Zhao, P., Jahn, B.-m. and Xu, B. (2017) Elemental and Sr-Nd isotopic geochemistry of
894 Cretaceous to Early Paleogene granites and volcanic rocks in the Sikhote-Alin Orogenic Belt

895 (Russian Far East): implications for the regional tectonic evolution. *Journal of Asian Earth Sciences*
896 146, 383-401.

897 Zhou, J.-B., Wilde, S.A., Zhao, G.-C. and Han, J. (2018) Nature and assembly of
898 microcontinental blocks within the Paleo-Asian Ocean. *Earth-Science Reviews* 186, 76-93.

899 Zhu, R.-X., Yang, J.-H. and Wu, F.-Y. (2012) Timing of destruction of the North China Craton.
900 *Lithos* 149, 51-60.

901 Zindler, A. and Hart, S. (1986) Chemical geodynamics. *Ann. Rev. Earth Planet. Sci.* 14, 493-571.

902 Zou, D., Liu, Y., Hu, Z., Gao, S., Zong, K., Xu, R., Deng, L., He, D. and Gao, C. (2014)
903 Pyroxenite and peridotite xenoliths from Hexigten, Inner Mongolia: Insights into the Paleo-Asian
904 Ocean subduction-related melt/fluid–peridotite interaction. *Geochimica et Cosmochimica Acta* 140,
905 435-454.

906

907

908

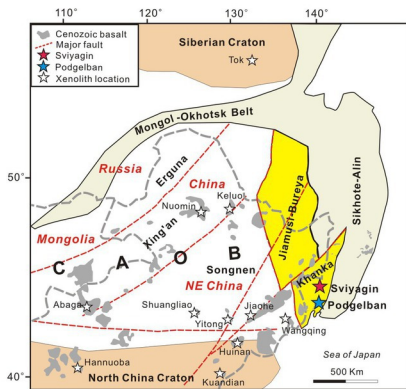


Fig.1

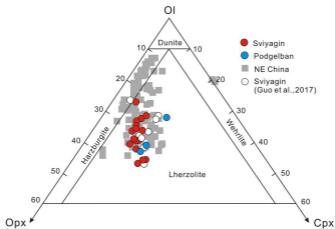


Fig.2

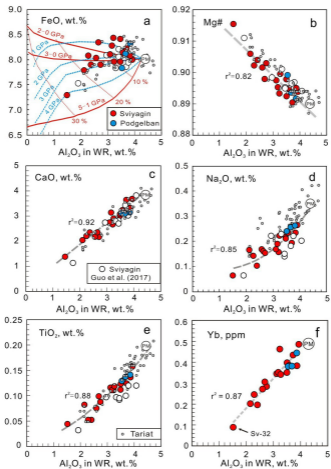


Fig.3

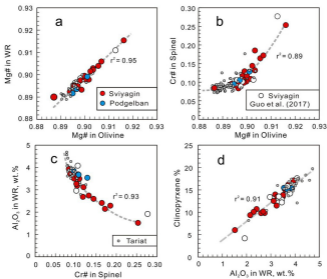


Fig.4

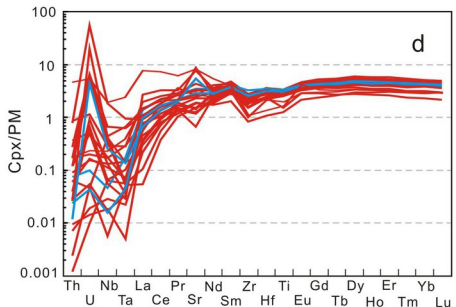
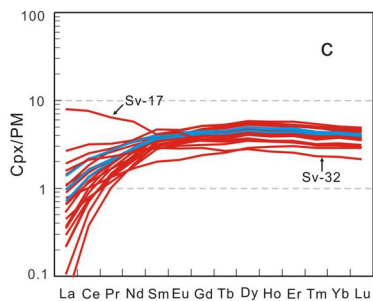
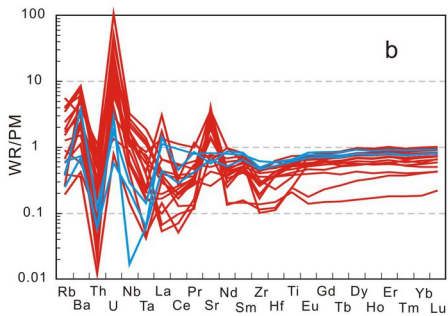
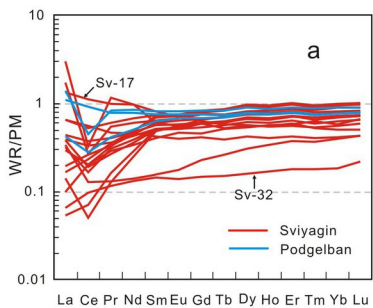


Fig. 5

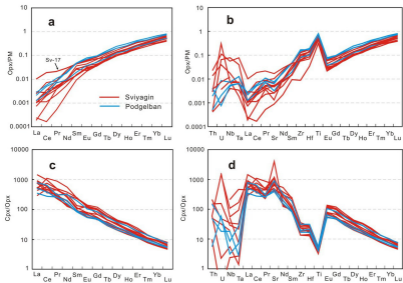


Fig.6

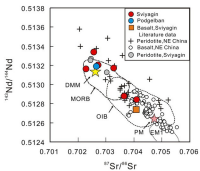


Fig.7

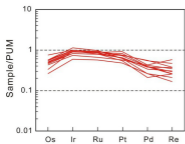


Fig.8

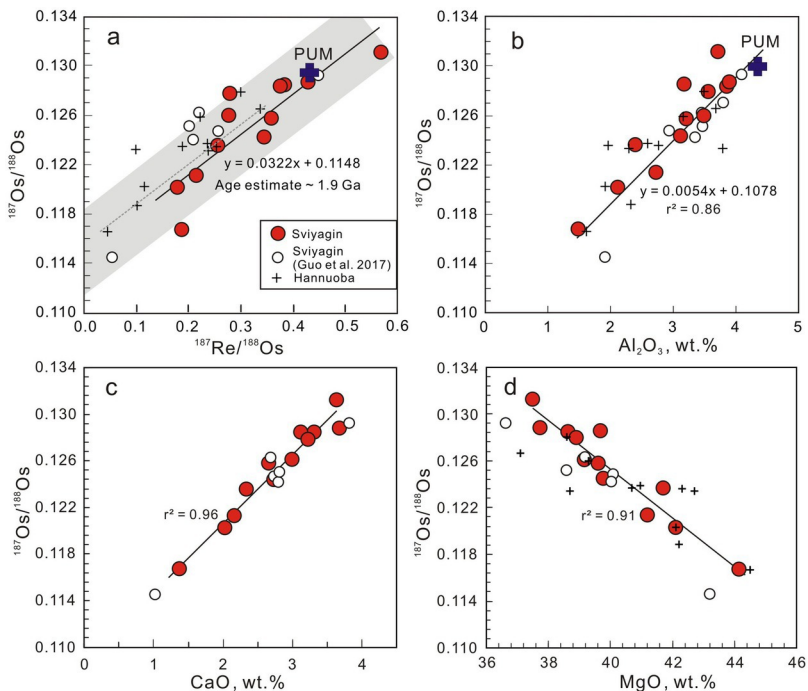


Fig. 9

Table 1

Summary of data for peridotite xenoliths from far eastern Russia

Sample no.	Al ₂ O ₃	CaO	Mg#	Mg#	Cr#	T	Calculated modal abundance				Sr-Nd	Re-Os
	WR, wt.%		WR	ol	spl	°C	ol	opx	cpx	sp		
<i>Sviyagin (spinel lherzolites)</i>												
Sv-4	2.74	2.17	0.903	0.903	0.13	933	61.8	26.9	9.8	1.6	+	+
Sv-7	2.41	2.35	0.904	0.906	0.16	953	66.4	21.1	10.7	1.7	+	+
Sv-8	n.d.	n.d.	n.d.	0.899	0.13	925	n.d.	n.d.	n.d.	n.d.	+	
Sv-9	3.93	3.68	0.894	0.896	0.08	892	52.4	28.2	17.1	2.4	+	+
Sv-13	3.24	2.66	0.893	0.899	0.10	845	57.0	28.7	11.5	2.1		+
Sv-14	2.29	2.21	0.902	0.903	0.19	898	65.8	23.0	10.1	1.4		
Sv-15	3.50	3.00	0.898	0.902	0.11	877	55.7	28.1	13.5	2.2		+
Sv-16	3.50	3.08	0.892	0.894	0.10	810	57.6	25.6	13.9	2.5		
Sv-17	2.60	2.17	0.902	0.902	0.14	995	63.0	25.2	9.8	1.3	+	
Sv-18	3.12	2.74	0.897	0.898	0.12	972	58.9	27.3	12.5	1.3		+
Sv-20	2.15	2.04	0.906	0.907	0.17	914	65.0	24.1	9.4	1.0		+
Sv-22	3.18	3.14	0.895	0.896	0.10	933	59.5	24.4	14.0	1.9		+
Sv-24	3.58	3.24	0.895	0.897	0.10	1000	56.2	26.4	15.1	2.0		+
Sv-27	2.68	2.35	0.898	0.900	0.12	816	62.9	24.8	10.2	1.7		
Sv-28	3.27	2.90	0.900	0.900	0.10	952	59.7	24.4	13.5	2.0		
Sv-29	3.86	3.32	0.895	0.895	0.09	970	55.9	25.9	15.3	2.5		+
Sv-32	1.52	1.38	0.915	0.916	0.25	988	72.0	21.5	6.0	0.9	+	+
8701-4	3.72	3.64	0.890	0.887	0.09	922	51.3	30.5	16.2	2.4		+
<i>Podgelban (spinel lherzolites)</i>												
Pod-1	3.54	3.13	0.899	0.901	0.13	993	65.7	16.5	15.5	3.2	+	
Pod-3	3.86	3.15	0.892	0.894	0.09	1054	57.2	25.7	15.4	2.5		
Pod-4	3.68	3.09	0.894	0.897	0.11	1033	55.1	28.5	15.1	2.2		

Samples Sv-9 and Sv-14 have porphyroblastic microstructure, all other samples are protogranular.

Sample Sv-8 was not analyzed for whole-rock composition.

Mg#, Mg/(Mg+Fe)_{at}; Cr#, Cr/(Al+Cr)_{at}; ol, olivine; opx, orthopyroxene; cpx, clinopyroxene; sp, spinel.

Equilibration temperatures (T) estimated using cpx-opx thermometry with a fixed P = 1.5 GPa (ES2).

Modal estimates obtained by least-squares method from whole-rock (WR) and mineral analyses (ES2).

n.d., not determined. (+) Samples with Sm-Nd and/or Re-Os isotope data

Table 2

Abundances of HSE, $^{187}\text{Re}/^{188}\text{Os}$ and $^{187}\text{Os}/^{188}\text{Os}$ ratios and model age estimates for peridotites in this study

Sample	Os ppb	Ir ppb	Ru ppb	Pt ppb	Pd ppb	Re ppb	$^{187}\text{Re}/^{188}\text{Os}$	$^{187}\text{Os}/^{188}\text{Os}$	2SE	T_{MA} Ga	T_{RD} Ga
Sv-4	2.187	3.48	6.12	4.67	2.68	0.088	0.217	0.12128	0.00006	2.25	1.14
Sv-7	1.955	3.20	5.59	6.10	2.78	0.090	0.257	0.12358	0.00007	2.00	0.82
Sv-9	2.107	3.35	6.46	5.69	3.84	0.162	0.433	0.12876	0.00007	19.10	0.12
Sv-13	1.784	2.83	5.46	4.88	2.63	0.128	0.361	0.12573	0.00008	3.06	0.53
Sv-15	1.832	3.11	5.98	4.74	2.36	0.104	0.279	0.12608	0.00007	1.34	0.48
Sv-18	1.277	3.22	5.54	4.09	1.47	0.089	0.348	0.12437	0.00008	3.51	0.72
Sv-20	2.902	3.45	6.35	5.43	2.76	0.100	0.182	0.12021	0.00005	2.18	1.28
Sv-22	1.883	2.84	5.45	5.51	3.87	0.130	0.385	0.12846	0.00006	1.35	0.16
Sv-24	1.001	2.06	3.89	3.61	1.82	0.058	0.284	0.12788	0.00007	0.68	0.24
Sv-29	1.663	2.55	4.56	4.32	2.97	0.120	0.380	0.12843	0.00006	1.25	0.16
Sv-32	2.179	3.90	6.77	4.62	1.83	0.073	0.192	0.11669	0.00009	3.10	1.75
8701-4	1.925	3.25	6.02	6.83	2.99	0.199	0.570	0.13122	0.00016	0.72	-0.22

SE, standard error. MA, model age; RD, rhenium-depletion age.

 T_{RD} and T_{MA} are calculated relative to the primitive upper mantle : $^{187}\text{Re}/^{188}\text{Os}=0.4353$; $^{187}\text{Os}/^{188}\text{Os}=0.1296$; $\lambda = 1.6660\text{E}-11$ Median T_{MA} value for all the samples is 2.1 Ga; average T_{MA} value (excepting the anomalously high value for Sv-9) is 1.95 Ga.